







Perceive-IR: Learning to Perceive Degradation Better for All-in-One Image Restoration

Xu Zhang , Jiaqi Ma , Guoli Wang , Qian Zhang , Huan Zhang , *Member, IEEE*, and Lefei Zhang , *Senior Member, IEEE*

Abstract—The limitations of task-specific and general image restoration methods for specific degradation have prompted the development of all-in-one image restoration techniques. However, the diversity of patterns among multiple degradation, along with the significant uncertainties in mapping between degraded images of different severities and their corresponding undistorted versions, pose significant challenges to the all-in-one restoration tasks. To address these challenges, we propose Perceive-IR, an all-in-one image restorer designed to achieve fine-grained quality control that enables restored images to more closely resemble their undistorted counterparts, regardless of the type or severity of degradation. Specifically, Perceive-IR contains two stages: (1) prompt learning stage and (2) restoration stage. In the prompt learning stage, we leverage prompt learning to acquire a fine-grained quality perceiver capable of distinguishing three-tier quality levels by constraining the prompt-image similarity in the CLIP perception space. Subsequently, this quality perceiver and difficulty-adaptive perceptual loss are integrated as a quality-aware learning strategy to realize fine-grained quality control in restoration stage. For the restoration stage, a semantic guidance module (SGM) and compact feature extraction (CFE) are proposed to further promote the restoration process by utilizing the robust semantic information from the pre-trained large scale vision models and distinguishing degradation-specific features. Extensive experiments demonstrate that our Perceive-IR outperforms state-of-the-art methods in all-in-one image restoration tasks and exhibit superior generalization ability when dealing with unseen tasks.

Index Terms—All-in-one image restoration, Prompt learning, Large vision model.

I. INTRODUCTION

IMAGE restoration, the process of which is to recover a clear image from its degraded version, has seen remarkable advancements with the emergence of deep learning. Traditionally, this challenge has been addressed by task-specific networks, each specifically designed and trained to handle a unique type of degradation. This targeted approach has yielded significant success across a spectrum of restoration tasks, e.g., denoising [1]–[3], dehazing [4]–[6], deraining [7]–[9], deblurring [10]–[12], and low-light enhancement [13]–[15].

Although task-specific methods have proven effective, their applicability is inherently restricted because they are designed

This work was in part supported by. (Xu Zhang and Jiaqi Ma contributed equally to this work.) (Corresponding author: Lefei Zhang.)

Xu Zhang, Jiaqi Ma, and Lefei Zhang are with the Institute of Artificial Intelligence, School of Computer Science, Wuhan University, Wuhan 430072, China. Lefei Zhang is also with the Hubei LuoJia Laboratory, Wuhan, China (e-mail: zx12220802@163.com; jiaqima@whu.edu.cn; zhanglefei@whu.edu.cn).

Guoli Wang and Qian Zhang are with the Horizon Robotics, Beijing 100083, China (e-mail: guoli.wang@horizon.cc; qian01.zhang@horizon.ai).

Huan Zhang is with the School of Information Engineering, Guangdong University of Technology, Guangzhou 510006, China (e-mail: huanzhang2021@gdut.edu.cn).

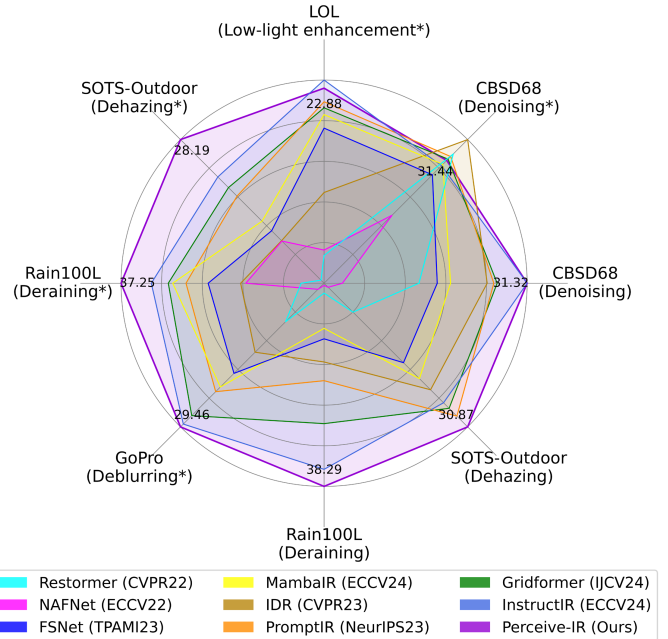


Fig. 1. PSNR comparisons with state-of-the-art all-in-one and general methods across two common all-in-one image restoration scenarios. * denotes results obtained under All-in-One (“Noise+Haze+Rain+Blur+Low-light”) training setting, while unmarked results are from All-in-One (“Noise+Haze+Rain”) training setting. Best viewed in color.

to address specific types of degradation. Once switched to other types of degradation scenarios, the effectiveness of these methods diminishes significantly. To overcome these limitations, general image restoration methods [16]–[22] which could handle various types of degradation, have been introduced. However, this approach typically requires training a separate network for each type of degradation. During the inference stage, model parameters need to be switched between different degradation scenarios to achieve optimal restoration performance. This process is not only resource-intensive but also impractical.

Recently, all-in-one image restoration methods [23]–[29] have surfaced as a potential solution to the aforementioned challenges. These methods are typically capable of addressing multiple degradation concurrently by employing various mechanisms. Early works, such as AirNet [23] and ADMS [24], obtained discriminative representations of degraded features by explicitly constructing degradation encoder or discriminator. Later, ProRes [25] and PromptIR [26] further improved the all-in-one restoration performance by injecting visual prompt information. Recently, some studies aim to leverage the powerful feature representation capabilities of pre-trained large-scale visual models such as CLIP [30] and

DINO [31] to promote texture information reconstruction and structural consistency maintenance. For instance, Tan *et al.* [32] explored the application of CLIP for adverse weather removal, demonstrating their effectiveness in restoring clear image under challenging weather conditions. Lin *et al.* [27] proposed a multi-task image restoration method guided by robust DINO features, which effectively enhances restoration quality under various degradation conditions.

Nevertheless, the substantial challenges in accurately mapping degraded images, which exhibit varying degrees of distortion, to their corresponding ground truths remain largely unresolved. Based on this, we develop a novel all-in-one image restoration method, which integrates quality-aware learning strategy alongside degradation-aware loss, leveraging the robust capabilities of large-scale vision models, enabling effective restoration of diverse degraded images with varying levels of degradation. First, we construct a fine-grained quality perceiver to discern three-tier image quality levels by constraining the prompt-image similarity in the CLIP perception space. Subsequently, this quality perceiver is integrated as a quality-aware learning strategy together with difficulty-adaptive perceptual loss to realize fine-grained quality control in restoration stage. For the restoration stage, a semantic guidance module (SGM) and compact feature extraction (CFE) are proposed to promote the restoration process. The SGM leverages robust semantic insights from large-scale vision models, while the CFE discerns and isolates degradation-specific features. As shown in Fig. 1, our proposed Perceive-IR demonstrates superior performance than state-of-the-art all-in-one and general methods under All-in-One training setting.

The contributions of this work can be summarized as follows:

- 1) We develop Perceive-IR, an all-in-one image restoration method that integrates quality-aware learning strategy alongside degradation-aware loss, leveraging the robust capabilities of large-scale vision models.
- 2) The proposed quality-aware learning strategy, which is grounded in prompt learning and difficulty-adaptive perceptual loss to realize fine-grained quality control, pushing the restored image towards the ground truth while pulling it away from samples under bad and medium quality levels.
- 3) We proposed a semantic guidance module which comprising a pre-trained DINO-v2 and the prompt guidance module to produce feature representations enriched with semantic and degradation priors.
- 4) Extensive experimental results across various restoration tasks demonstrate the superior performance of our Perceive-IR, including image denoising, dehazing, deraining, deblurring, and low-light enhancement tasks.

II. RELATED WORK

A. All-in-one restoration

All-in-one restoration [23]–[29], [32]–[37] aims to recover clean images from multiple degraded images through a unified model, has grown to be a promising field of low-level vision tasks. Compared to task-specific [1]–[15] and general [16]–[22], [38]–[40] image restoration, all-in-one restoration is more advantageous in terms of model storage efficiency and

practical applications. The main challenge lies in using a single set of model parameters to handle various types of degradation and accurately restore the corresponding components. To achieve this, AirNet [23] proposed learning discriminative degradation representation using contrastive learning. IDR [34] took a different approach by utilizing a two-stage ingredients-oriented restoration network. PromptIR [26] and ProRes [25] further enhanced the network’s ability to handle multiple degradation through vision prompts. More recently, CLIP-AWR [32], DA-CLIP [29], and DINO-IR [27] leveraged pre-trained large-scale vision models to excel in all-in-one restoration tasks.

However, in practice, degraded images often suffer from varying levels of corruption. The above methods may fall into the trap of processing these images with the same restoration effort, resulting in sub-optimal performance. Based on this observation, Chen *et al.* [36] designed a blind all-in-one image restoration method namely UtilityIR with learning an image quality ranker. However, it depends on the simple image quality metric, *i.e.*, PSNR, and is susceptible to variations in certain parameters. In comparison, our method focuses on leveraging CLIP’s zero-shot capability to construct a more robust quality perceiver to achieve fine-grained quality control of the restored images.

B. Prompt Learning

In recent years, prompt learning as an emerging learning paradigm has seen significant advancements in the field of natural language processing [41]–[43]. Its effectiveness has led to its widespread application in vision-related tasks [44]–[48]. The core idea is to enable pre-trained models to better understand and perform downstream tasks by constructing specific prompts. In natural language processing, these prompts are usually given in the form of text, whereas in computer vision, they may involve images, text, or other forms of data.

In the image restoration, PromptIR [26] and ProRes [25] firstly introduced prompt learning to all-in-one image restoration, further enhancing the restoration capability of the model with vision prompts. Recently, CLIP-LIT [49] has shown that initializing textual prompts in CLIP can aid in extracting more accurate low-level image representations. However, relying solely on distinguishing between positive and negative prompts may fail to effectively guide the restoration process towards achieving undistorted images. This is because the vast spectrum of possibilities between the two prompts can complicate the accurate mapping of degraded images to their pristine counterparts. To address this, we propose an effective prompt learning approach by further differentiating among three-tier prompt pairs to enable more nuanced and precise control of the restoration process towards the undistorted counterparts.

C. Large-scale Vision Models

Large-scale vision models (LVMS) have shown powerful robust feature representation and zero-shot transfer capabilities in various tasks. For example, CLIP [30] has been successfully applied on various downstream tasks [50]–[52] due to its amazing semantic alignment ability between vision and language. As the self-supervised ViT model, DINO [31] and DINO-v2 [53] have demonstrated effectiveness across multiple

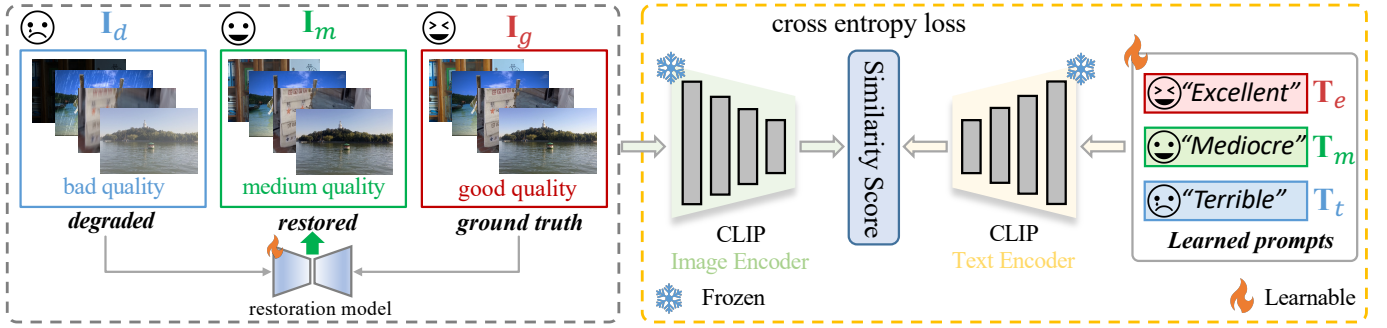


Fig. 2. In the proposed prompt learning stage, we initialize and train textual prompts using image-text pairs categorized into three tiers of quality. These prompts are trained with cross-entropy loss in the CLIP model. Once trained, the learned prompts are fixed and used to guide the restoration of high-quality images during the subsequent restoration stage.

tasks [54], [55] and eliminate the need for labeled input data. Since these LVMs can learn useful prior knowledge from external hyper-scale datasets, a similar pipeline that draws on pre-trained LVMs has become increasingly popular in the low-level community [27], [29], [32]. Inspired by the aforementioned studies, in this paper, we utilize the semantic prior knowledge and structural information mined by the proposed DINO-v2-based semantic guidance module to guide the restoration process.

III. METHOD

A. Overview Pipeline

Our Perceive-IR contains two stages: a prompt learning stage and a restoration stage. In the prompt learning stage, we initialize and train textual prompts using image-text pairs categorized into three-tier of quality by constraining the text-image similarity in the CLIP perception space. The learned prompts are fixed and then used to guide the restoration processing during the subsequent stage. In the restoration stage, we use compact feature extraction (CFE) to learn distinct degradation representations. These representations are then concatenated with semantic priors extracted by pre-trained DINO-v2 encoder. These concatenated features modulate the output features of the decoder within the prompt guidance module (PGM). The calibrated features are further emphasized by the prior guidance cross attention (PGCA) to extract and convey structural semantic information. Moreover, we utilize quality-aware learning strategy which contains CLIP-aware loss and difficulty-adaptive perceptual loss to realize fine-grained quality control and guide the restoration of high-quality images.

B. Prompt Learning Stage

The process of prompt learning stage is shown in Fig. 2. We use the CLIP model to learn the three types of prompts, *i.e.*, “terrible”, “mediocre”, and “excellent”, corresponding to the three-tier quality levels of images to the CLIP image encoder, *i.e.*, bad, medium, and good quality images. Specifically, we divide the degraded inputs equally into two subsets. Then, we train a restoration model, *i.e.*, Restormer [20] to obtain the restored images \mathbf{I}_m via cross-validation strategy. The restored images are regarded as the medium quality images. After that, given a bad quality image $\mathbf{I}_d \in \mathbb{R}^{H \times W \times 3}$, a medium quality image $\mathbf{I}_m \in \mathbb{R}^{H \times W \times 3}$, and a good quality $\mathbf{I}_g \in \mathbb{R}^{H \times W \times 3}$, we randomly initialize a “terrible” textual prompt $\mathbf{T}_t \in \mathbb{R}^{N \times 512}$,

a “mediocre” textual prompt $\mathbf{T}_m \in \mathbb{R}^{N \times 512}$, and a “excellent” textual prompt $\mathbf{T}_e \in \mathbb{R}^{N \times 512}$. N represents the number of embedded tokens in each prompt. Then, we feed the bad, medium, and good quality images \mathbf{I}_d , \mathbf{I}_m , and \mathbf{I}_g to the CLIP image encoder to obtain their latent encoding. Meanwhile, we extract the latent encodings of the “excellent”, “mediocre”, and “terrible” textual prompts by feeding them to the CLIP text encoder. Based on the text-image similarity in the CLIP latent space, we use the cross entropy loss \mathcal{L}_{ce} of classifying the bad, medium, and good quality images to learn these prompts. The \mathcal{L}_{ce} can be described as

$$\mathcal{L}_{ce} = -\frac{1}{3} \sum_{i \in \{d, m, g\}} \sum_{j \in \{e, m, t\}} \mathcal{Y}_{ij} \log \left(\frac{\exp(\mathcal{S}(\Phi_{\mathcal{I}}(\mathbf{I}_i), \Phi_{\mathcal{T}}(\mathbf{T}_j)))}{\sum_{k \in \{e, m, t\}} \exp(\mathcal{S}(\Phi_{\mathcal{I}}(\mathbf{I}_i), \Phi_{\mathcal{T}}(\mathbf{T}_k)))} \right), \quad (1)$$

where $\mathcal{S}(\cdot, \cdot)$ denotes cosine similarity and \mathcal{Y}_{ij} is the label of the current image \mathbf{I}_i ; $\Phi_{\mathcal{I}}(\cdot)$ and $\Phi_{\mathcal{T}}(\cdot)$ denote CLIP image encoder and CLIP text encoder, respectively.

C. Restoration Stage

Restoration Branch. As shown in Fig. 3, given a degraded input $\mathbf{I}_d \in \mathbb{R}^{H \times W \times 3}$, we first applies a 3×3 convolution to extract shallow embeddings $\mathbf{X}_s \in \mathbb{R}^{H \times W \times C}$, where $H \times W$ denotes the spatial dimension and C is the number of channels. Next, the shallow features \mathbf{X}_s are gradually and hierarchically encoded into deep features $\mathbf{X}_l^{e, d} \in \mathbb{R}^{\frac{H}{2^{l-1}} \times \frac{W}{2^{l-1}} \times 2^{l-1} C}$. After encoding the degraded input into latent features $\mathbf{X}_4 \in \mathbb{R}^{\frac{H}{8} \times \frac{W}{8} \times 8C}$, the decoder progressively recovers the high-resolution representations. Finally, a 3×3 convolution is applied to reconstruct restored image $\mathbf{I}_r \in \mathbb{R}^{H \times W \times 3}$.

In the restoration branch, we choose Restormer [20] as backbone. Specifically, in the encoder layer, we integrate Multi-Dconv Head Transposed Attention (MDTA) [20] and Gated-Dconv Feed-Forward Network (GDFN) [20] to jointly construct the Transformer Block (TB). In the latent and decoder layers, we introduce the Prior Guidance Cross Attention (PGCA) and GDFN to jointly construct the Enhanced Transformer Block (ETB). The process of restoration branch can be described as

$$\mathcal{F}_{tb}(\mathbf{X}_l^e) = \mathcal{F}_{gdfn}(\mathcal{F}_{mdta}(\mathbf{X}_l^e)), \quad (2)$$

$$\mathcal{F}_{etb}(\mathbf{X}_l^d, \mathbf{Y}_l) = \mathcal{F}_{gdfn}(\mathcal{F}_{pgca}(\mathbf{X}_l^d, \mathbf{Y}_l)), \quad (3)$$

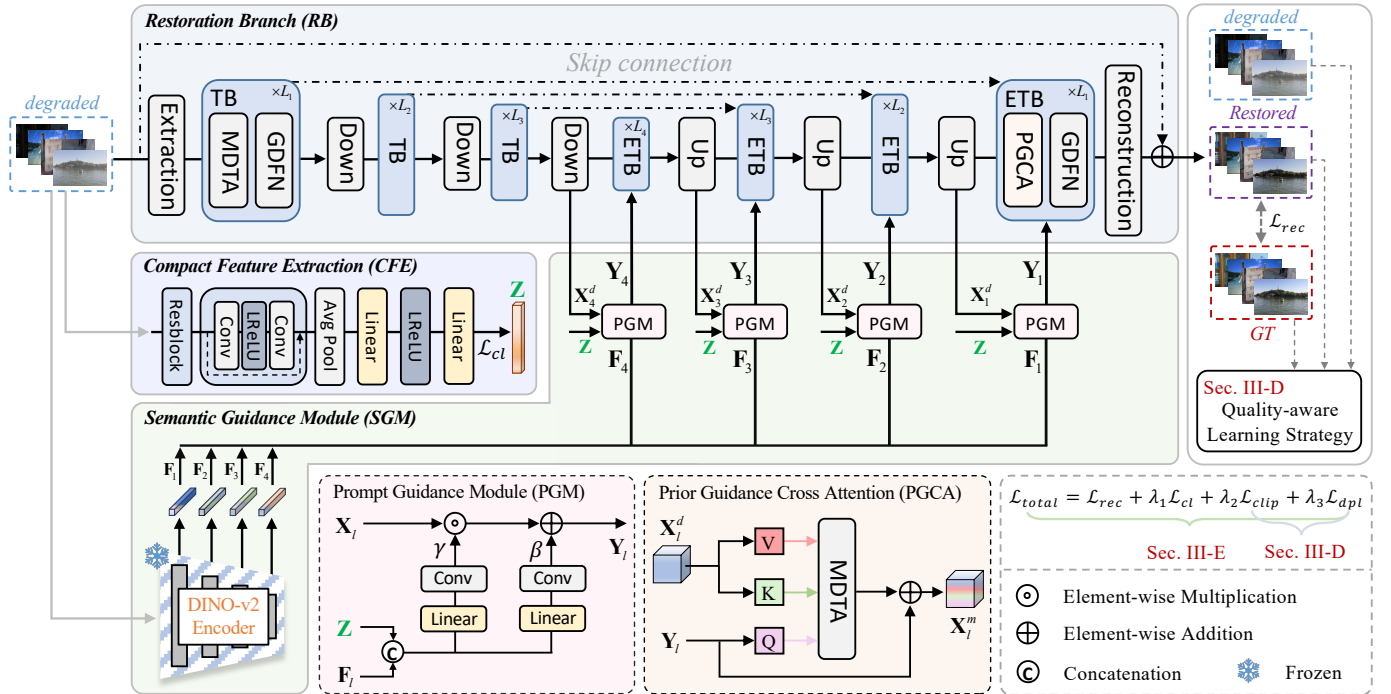


Fig. 3. The proposed restoration stage consists of: (a) Restoration Branch (RB): A 4-level U-shaped encoder-decoder structure that incorporates Transformer Block (TB) [20] in the encoder and Enhanced Transformer Block (ETB) in the decoder. (b) Compact Feature Extraction (CFE): A module designed to generate distinctive degradation representation. (c) Semantic Guidance Module (SGM): Comprising a pre-trained DINO-v2 [53] and the Prompt Guidance Module (PGM) to produce feature representations enriched with semantic and degradation priors.

$$\mathbf{I}_r = \text{Conv} \left(\mathcal{F}_{etb}^{4,3,2,1} \left(\mathcal{F}_{tb}^{1,2,3} \left(\text{Conv}(\mathbf{I}_d) \downarrow_{\times 2}, \mathbf{Y}_l \right) \uparrow_{\times 2} \right) \right) + \mathbf{I}_d, \quad (4)$$

where $\mathcal{F}_{gdfn}(\cdot)$, $\mathcal{F}_{mdta}(\cdot)$, $\mathcal{F}_{pgca}(\cdot)$, $\mathcal{F}_{tb}(\cdot)$, and $\mathcal{F}_{etb}(\cdot)$ indicate GDFN, MDTA, PGCA, TB, and ETB processes, respectively; \mathbf{X}_l^e denotes output of l -th encoder layer and \mathbf{X}_l^d represents input of l -th decoder layer, respectively; $\text{Conv}(\cdot)$ indicates 3×3 convolution operation and \mathbf{Y}_l denotes output of prompt guidance module; \downarrow and \uparrow indicate down-sampling and up-sampling, respectively.

Compact Feature Extraction. In the restoration stage, we propose Compact Feature Extraction (CFE) to extract a compact degradation representation $\mathbf{Z} \in \mathbb{R}^{1 \times 128}$. Then, we utilize the degradation loss \mathcal{L}_{cl} (as detailed in Sec. III-E) to optimize CFE by leveraging the consistency of images with the same degradation and the inconsistency across different degradation. After that, \mathbf{Z} will be concatenated with the multi-scale features \mathbf{F}_l extracted by pre-trained large vision model. The deep feature \mathbf{X}_l^d and the concatenated feature will perform affine transformation in Prompt Guidance Module (PGM) to obtain \mathbf{Y}_l . Subsequently, the \mathbf{Y}_l is employed to execute cross-attention within the Enhanced Transformer Block (ETB).

Semantic Guidance Module. Recently, large-scale vision models (e.g., DINO family [31], [53]) have demonstrated its potential in a series of visual downstream tasks [54], [55] in a self-supervised manner. DINO-v2, as an improved version of DINO, can provide more powerful feature representation thanks to pre-training on more than one million data. To this end, we employ the DINO-v2 to extract useful semantic feature priors from degraded images. Additionally, a prompt guidance module (PGM) is designed to help the network better capture and preserve structural semantic information. As

shown in Fig. 3, given a degraded image \mathbf{I}_d , it goes through the pre-trained DINO-v2 encoder and outputs four different levels of semantic features $\mathbf{F}_l \in \mathbb{R}^{1 \times 768}$ ($l = 1, 2, 3, 4$). This process can be described as

$$\mathbf{F}_1, \mathbf{F}_2, \mathbf{F}_3, \mathbf{F}_4 = \mathcal{D}_i(\mathbf{I}_d), \quad i = 1, 4, 8, 12, \quad (5)$$

where $\mathcal{D}_i(\cdot)$ denotes i -th layer of DINO-v2 encoder. Then, the semantic prior and learned degradation representation \mathbf{Z} are exploited to generate reliable content to guide the restoration by PGM. The modulated feature \mathbf{Y}_l is transmitted to prior guidance cross attention (PGCA) to guide the restoration branch. Specifically, we take \mathbf{Y}_l as query to perform the cross-attention. The above process can be expressed as

$$\mathbf{Y}_l = \mathcal{F}_{pgm}(\mathbf{F}_l, \mathbf{Z}, \mathbf{X}_l^d), \quad (6)$$

$$\text{CrossAtt}(\mathbf{Y}_l, \mathbf{X}_l^d, \mathbf{X}_l^d) = \text{Softmax}(\hat{\mathbf{Q}} \otimes \hat{\mathbf{K}}/\alpha) \otimes \hat{\mathbf{V}}, \quad (7)$$

$$\mathbf{X}_l^m = \mathcal{F}_{mdta}(\text{CrossAtt}(\mathbf{Y}_l, \mathbf{X}_l^d, \mathbf{X}_l^d)) + \mathbf{Y}_l, \quad (8)$$

where \mathcal{F}_{pgm} indicates PGM process; \otimes denotes matrix multiplication.

D. Quality-aware Learning Strategy

CLIP-aware Loss. As illustrated in Fig. 4, given the learned text prompts obtained from the prompt learning stage, we first fix these prompts and then train the restoration model using the CLIP-aware loss \mathcal{L}_{clip} . The \mathcal{L}_{clip} can be described as

$$\mathcal{L}_{clip} = 1 - \frac{\exp \left(\mathcal{S}(\Phi_{\mathcal{I}}(\mathbf{I}_r), \Phi_{\mathcal{T}}(\mathbf{T}_e)) \right)}{\sum_{k \in \{e, m, t\}} \exp \left(\mathcal{S}(\Phi_{\mathcal{I}}(\mathbf{I}_r), \Phi_{\mathcal{T}}(\mathbf{T}_k)) \right)}, \quad (9)$$

where $\mathcal{S}(\cdot, \cdot)$ denotes cosine similarity. The \mathcal{L}_{clip} is to minimize the gap between the restored images \mathbf{I}_r and the ‘‘excellent’’ prompt \mathbf{T}_e , while maximizing the gap between \mathbf{I}_r

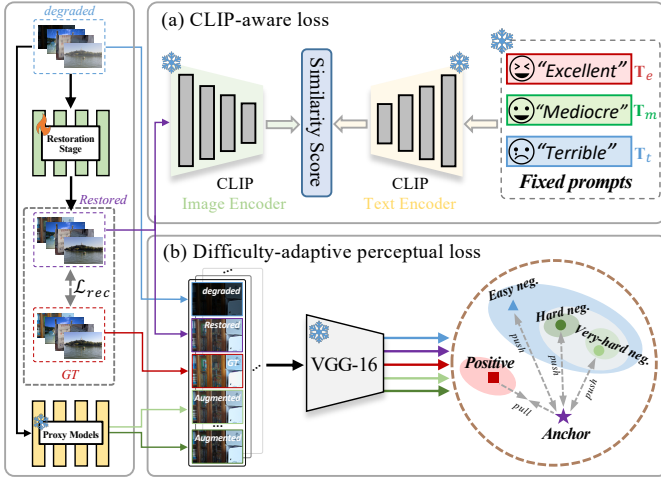


Fig. 4. The proposed quality-aware learning strategy contains two components. (a) The CLIP-aware loss and (b) The difficulty-adaptive perceptual loss.

with the “mediocre” prompt \mathbf{T}_m and “terrible” prompt \mathbf{T}_t , respectively. It emphasizes pulling the restored results closer to ground truth, guiding the model to generate high-quality images.

Difficulty-adaptive Perceptual Loss. Using contrastive regularization has been demonstrated as an effective way of improving image restoration performance [56], [57]. Based on this, we introduce the difficulty-adaptive perceptual loss to dynamically adjust its behavior based on the difficulty level of the restoration process. It effectively handles both easy and hard samples, ensuring that the network focuses appropriately on challenging samples while efficiently processing easy cases. As shown in Fig. 4, the image predicted \mathbf{I}_r by the network serves as the anchor, the reference image \mathbf{I}_g as positive sample, the degraded \mathbf{I}_d as easy negative sample, and the augmented images \mathbf{I}_q from proxy restoration models (e.g., InstructIR [28], PromptIR [26], FSNet [21], and MambaIR [40]) as hard or very-hard negative samples.

Specifically, at the beginning of the k -th epoch, we evaluate the performance of network by calculating the average PSNR score and categorize the non-easy negative sample as a very-hard sample if its PSNR surpasses the current network performance, otherwise, it is classified as hard negative sample. Then, the weight \mathcal{O}_k of the k -th epoch assigned to a non-easy negative sample \mathcal{N}_q , are defined as

$$\mathcal{O}_k(\mathcal{N}_q) = \begin{cases} 1 + \gamma, & \text{avgPSNR}(\mathbf{I}_r, \Theta_{k-1}) \geq \text{PSNR}(\mathcal{N}_q), \\ 1 - \gamma, & \text{otherwise,} \end{cases} \quad (10)$$

where $q = 1, 2, \dots, z$; z is the number of non-easy negatives, and γ is a hyperparameter set to 0.25; Θ_{k-1} represents the model weights from the $(k-1)$ -th epoch. The weights of hard and very-hard negatives are set to $1 + \gamma$ and $1 - \gamma$, respectively. Based on this, the proposed \mathcal{L}_{dpl} can be written as

$$\mathcal{L}_{dpl} = \sum_{i=3,7,11,15} \xi_i \frac{\mathcal{M}_i(\mathbf{I}_g, \mathbf{I}_r)}{\lambda \mathcal{M}_i(\mathbf{I}_d, \mathbf{I}_r) + \sum_{q=1}^z \mathcal{O}_k(\mathcal{N}_q) \mathcal{M}_i(\mathcal{N}_q, \mathbf{I}_r)}, \quad (11)$$

where $\mathcal{M}_i(\cdot, \cdot) = \|\mathcal{V}_i(\cdot) - \mathcal{V}_i(\cdot)\|_1$; $\mathcal{V}_i(\cdot)$ represents the i -th latent feature extracted from the pre-trained VGG-16 [58]. We use the latent features of 3-rd, 7-th, 11-th, 15-th layers from VGG-16 to calculate $\mathcal{M}_i(\cdot, \cdot)$. We assign a fixed weight λ to

the easy negative and set $\lambda = 2$. $\{\xi_i\}$ represents the set of hyperparameters, we set ξ_i ($i = 3, 7, 11, 15$) to $\frac{1}{12}$, $\frac{1}{6}$, $\frac{1}{3}$, and 1, respectively.

E. Training Loss

In the prompt learning stage, we use \mathcal{L}_{ce} to learn the initial text prompt pairs. In the restoration stage, we first utilize the CFE and introduce a degradation-aware loss \mathcal{L}_{cl} to learn degradation representations. The \mathcal{L}_{cl} can be written as

$$\mathcal{L}_{cl} = -\log \frac{\exp(\mathcal{S}(\mathbf{Z}, \mathbf{Z}^+)/\tau)}{\exp(\mathcal{S}(\mathbf{Z}, \mathbf{Z}^+)/\tau) + \sum_{i=1}^n \exp(\mathcal{S}(\mathbf{Z}, \mathbf{Z}_i^-)/\tau)}, \quad (12)$$

where n and τ indicate the number of negative samples and the temperature, respectively. Given several images containing different degradation types, we randomly crop two patches of the same resolution on an image and let them be positive samples, while letting patches of different degradation types be negative samples. Then, input them into CFE to get anchor feature \mathbf{Z} , positive feature \mathbf{Z}^+ , and negative feature \mathbf{Z}^- .

The total loss of the restoration stage can be described as

$$\mathcal{L}_{total} = \mathcal{L}_{rec} + \lambda_1 \mathcal{L}_{cl} + \lambda_2 \mathcal{L}_{clip} + \lambda_3 \mathcal{L}_{dpl}, \quad (13)$$

where \mathcal{L}_{rec} is \mathcal{L}_1 loss; λ_1 , λ_2 , and λ_3 are hyperparameters to make a balance among the total loss.

IV. EXPERIMENTS

A. Experimental Setup

Datasets. Following [23], [26], [34], we differentiate the training setups into “All-in-One” and “One-by-One” based on whether datasets are combined for mixed training. In our study, we summarise two common mixed degradation: “Noise+Haze+Rain (N+H+R)” and “Noise+Haze+Rain+Blur+Low-light (N+H+R+B+L)”. Under the “One-by-One” setting, the model is trained and tested using datasets from a single image restoration task at a time. Under the “All-in-One” setting, the model is trained and tested using mixed datasets from multiple image restoration tasks.

In Tab. I, we detail the training and testing datasets used in our experiments. For single-task image restoration, **i)** Image denoising: we conduct training using a merged dataset of BSD400 [59] and WED [60] with 400 and 4,744 clear images, respectively. Noisy images are generated with Gaussian noise ($\sigma \in \{15, 25, 50\}$). Testing is performed on CBSD68 [61], Urban100 [62], and Kodak24 [63] datasets. **ii)** Image dehazing: we use the OTS dataset of RESIDE- β [64] with 72,135 pairs for training and 500 images from SOTS-Outdoor [64] dataset for testing. **iii)** Image deraining: we use the Rain100L [65] dataset with 200 pairs of images for training and 100 pairs for testing. **iv)** Image deblurring: we train the model on the GoPro [11] dataset, which contains 2,103 pairs for training and 1,111 pairs for testing. **v)** Low-light enhancement: we use the LOL [13] dataset, which contains 485 pairs for training and 15 pairs for testing. For multi-task image restoration, we trained on a mixed dataset containing multiple degradation and tested one by one on the dataset containing a single type of degradation. **Evaluation Metrics.** For evaluation, we present the values of the Peak Signal to Noise Ratio (PSNR) and Structural Similarity (SSIM). In addition, for the underwater image

TABLE I
DATASET SUMMARY UNDER TWO TRAINING SETTINGS.

Setting	Degradation	Training dataset (Number)	Testing dataset (Number)
One-by-One (Single-task)	Noise (N)	N : BSD400 [59]+WED [60] (400+4744)	N : CBSD68 [61]+Urban100 [62] +Kodak24 [63] (68+100+24)
	Haze (H)	H : RESIDE- β -OTS [64] (72135)	H : SOTS-Outdoor [64] (500)
	Rain (R)	R : Rain100L [65] (200)	R : Rain100L [65] (100)
	Blur (B)	B : GoPro [11] (2103)	B : GoPro [11] (1111)
	Low-light (L)	L : LOL [13] (485)	L : LOL [13] (15)
All-in-One (Multi-task)	N+H+R	BSD400 [59]+WED [60]+RESIDE- β -OTS [64]+Rain100L [65] Number : 400+4744+72135+200 Total : 77479	N : CBSD68 [61] (68) H : SOTS-Outdoor [64] (500) R : Rain100L [65] (100)
	N+H+R+B+L	BSD400 [59]+WED [60]+RESIDE- β -OTS [64]+Rain100L [65] +GoPro [11]+LOL [13] Number : 400+4744+72135+200+2103+485 Total : 80067	N : CBSD68 [61] (68) H : SOTS-Outdoor [64] (500) R : Rain100L [65] (100) B : GoPro [11] (1111) L : LOL [13] (15)

enhancement task, we extend our report to include Learned Perceptual Image Patch Similarity (LPIPS) [66], Underwater Colour Image Quality Evaluation Metric (UCIQE) [67], and Underwater Image Quality Measure (UIQM) [68] scores. In tables, the best and second-best scores are highlighted in **bold** and underline, respectively. PSNR/SSIM metrics are reported on the RGB images.

Baselines. In the All-in-One (“N+H+R”) setting, we select four task-specific methods: LPNet [69], ADFNet [70], DehazeFormer [6], and DRSformer [9]; five general methods: MPRNet [16], Restormer [20], NAFNet [19], FSNet [21], and MambaIR [40]. and seven all-in-one methods: DL [71], AirNet [23], IDR [34], NDR [35], PromptIR [26], Gridformer [37] and InstructIR [28]. In the All-in-One (“N+H+R+B+L”) setting, we add task-specific methods like HI-Diff [72] and Retinexformer [15]; general methods such as DGUNet [38], MIRNet-v2 [18], and SwinIR [17], as well as all-in-one methods like Transweather [73], and TAPE [33].

In the One-by-One setting, we focus on adjustments to task-specific methods. For denoising, we employ DnCNN [1], FFDNet [2], BRDNet [3], and ADFNet [70]. For dehazing, we utilize DehazeNet [4], AODNet [74], FDGAN [5], and DehazeFormer [6]. For deraining, we apply UMR [7], MSPFN [8], LPNet [69], and DRSformer [9]. For image deblurring, we leverage DeblurGAN [10], Stripformer [12], and HI-Diff [72]. Lastly, for low-light image enhancement, we incorporate Retinex-Net [13], URetinex [14], and Retinexformer [15]. In addition to these methods, we also report results from some representative general and all-in-one methods trained in the One-by-One setting.

Implementation Details. For the prompt learning stage, we employ the CLIP [30] model with ViT-B/32 as the backbone. We train Restormer [20] for 100K iterations with a learning rate of 2×10^{-4} . The number of embedded tokens N in each learnable prompt is set to 16, and the prompt initialization is set to 100K iterations with a learning rate of 4×10^{-5} and the batch size is set to 32. For the restoration stage, We chose Restormer as the restoration backbone of Perceive-IR and DINO-v2 [53] base version as the semantic guidance module. We adopt a similar setting to the original Restormer. From level-1 to level-4, the numbers of TB and ETB are [4, 6, 6, 8], attention heads in MDTA and PGCA are both [1, 2, 4, 8], and the channel numbers are [48, 96, 192, 384]. We utilize

AdamW optimizer with $\beta_1 = 0.9$ and $\beta_2 = 0.999$ to optimize the network. The learning rate is set to 2×10^{-4} with a total batch size of 6 for 400K iterations. The weighting parameters for \mathcal{L}_{total} are: $\lambda_1 = 0.1$, $\lambda_2 = 0.05$, and $\lambda_3 = 0.1$.

All experiments are conducted on 8 NVIDIA GeForce RTX 3090 GPUs. During training, we utilize cropped patches of size 128×128 as input, and random horizontal and vertical flips are applied to augment the training data.

B. All-in-One Restoration Results

Tab. II presents the overall performance of Perceive-IR and other state-of-the-art methods under the All-in-One “Noise+Haze+Rain” training setting. It can be observed that the all-in-one methods basically perform better than general methods and task-specific methods. Particularly, in terms of overall performance, our Perceive-IR exhibits superior results compared with PromptIR [26] by over 0.57 dB/0.004 on average in PSNR/SSIM while utilizing the same backbone of Restormer [20]. Compared to the latest methods, Gridformer [37] and InstructIR [28], Perceive-IR also demonstrates a PSNR/SSIM improvement of 0.44 dB/0.005 and 0.20 dB/0.004, respectively.

As indicated in Tab. III, when extending to the more challenging “Noise+Haze+Rain+Blur+Low-light” setting, our Perceive-IR still exhibit superior results compared with PromptIR, Gridformer, and InstructIR by over 0.69 dB/0.005, 0.51 dB/0.005, and 0.29 dB/0.002 on average in PSNR/SSIM, respectively. It can be observed that as the number of degradation types increases, the advantages of the comparative all-in-one methods become faint over general image restoration methods. By contrast, by incorporating both type-aware and quality-aware perception, and the delicate incorporation of the DINO-v2-based semantic prior guidance module, Perceive-IR still maintains good performance.

C. One-by-One Restoration Results

In this part, we evaluate Perceive-IR under One-by-One setting. As shown in Tab. IV, compared to the state-of-the-art (SOTA) task-specific denoising method ADFNet [70] and the SOTA general image restoration method FSNet [21], Perceive-IR surpasses them by 0.17 dB and 0.29 dB in PSNR, respectively, at a noise level of 15 on the CBSD68 and Urban100 datasets. As shown in Tab. V, while Perceive-IR demonstrates highly competitive performance in dehazing and

TABLE II

PERFORMANCE COMPARISON IN ALL-IN-ONE (“N+H+R”) SETTING WITH TASK-SPECIFIC, GENERAL, AND ALL-IN-ONE IMAGE RESTORATION METHODS. THE REPORTED RESULTS ARE PARTIALLY BASED ON NDR [35] AND PROMPTIR [26]. * DENOTES A MODEL THAT HAS BEEN RETRAINED.

Type	Method	Denoising (CBSD68 [61])			Dehazing	Deraining	Average	Params (M)
		$\sigma = 15$	$\sigma = 25$	$\sigma = 50$	SOTS [64]	Rain100L [65]		
Specific	(CVPR'19) LPNet [69]	26.47/0.778	24.77/0.748	21.26/0.552	20.84/0.828	24.88/0.784	23.64/0.738	2.84
	(AAAI'23) ADFNet* [70]	33.76/0.929	30.83/0.871	27.75/0.793	28.13/0.961	34.24/0.965	30.94/0.904	7.65
	(TIP'23) DehazeFormer* [6]	33.01/0.914	30.14/0.858	27.37/0.779	29.58/0.970	35.37/0.969	31.09/0.898	25.44
	(CVPR'23) DRSformer* [9]	33.28/0.921	30.55/0.862	27.58/0.786	29.02/0.968	35.89/0.970	31.26/0.902	33.72
General	(CVPR'21) MPRNet [16]	33.27/0.920	30.76/0.871	27.29/0.761	28.00/0.958	33.86/0.958	30.63/0.894	15.74
	(CVPR'22) Restormer [20]	33.72/0.930	30.67/0.865	27.63/0.792	27.78/0.958	33.78/0.958	30.75/0.901	26.13
	(ECCV'22) NAFNet [19]	33.03/0.918	30.47/0.865	27.12/0.754	24.11/0.928	33.64/0.956	29.67/0.844	17.11
	(TPAMI'23) FSNet* [21]	33.81/0.930	30.84/0.872	27.69/0.792	29.14/0.968	35.61/0.969	31.42/0.906	13.28
	(ECCV'24) MambaIR* [40]	33.88/0.931	30.95/0.874	27.74/0.793	29.57/0.970	35.42/0.969	31.51/0.907	26.78
All-in-One	(TPAMI'19) DL [71]	33.05/0.914	30.41/0.861	26.90/0.740	26.92/0.391	32.62/0.931	29.98/0.875	2.09
	(CVPR'22) AirNet [23]	33.92/0.932	31.26/0.888	28.00/0.797	27.94/0.962	34.90/0.967	31.20/0.910	8.93
	(CVPR'23) IDR* [34]	33.89/0.931	31.32/0.884	28.04/0.798	29.87/0.970	36.03/0.971	31.83/0.911	15.34
	(ArXiv'23) ProRes [25]	32.10/0.907	30.18/0.863	27.58/0.779	28.38/0.938	33.68/0.954	30.38/0.888	370.63
	(ArXiv'23) NDR [35]	34.01/0.932	31.36/0.887	28.10/0.798	28.64/0.962	35.42/0.969	31.51/0.910	-
	(NeurIPS'23) PromptIR [26]	33.98/0.933	31.31/0.888	28.06/0.799	30.58/0.974	36.37/0.972	32.06/0.913	32.96
	(IJCV'24) Gridformer* [37]	33.93/0.931	31.37/0.887	28.11/0.801	30.37/0.970	37.15/0.972	32.19/0.912	34.07
	(ECCV'24) InstructIR [28]	34.15/0.933	31.52/0.890	28.30/0.804	30.22/0.959	37.98/0.978	32.43/0.913	15.80
	Perceive-IR (Ours)	34.13/0.934	31.53/0.890	28.31/0.804	30.87/0.975	38.29/0.980	32.63/0.917	42.02



Fig. 5. Visual comparisons of Perceive-IR with state-of-the-art all-in-one methods for All-in-One (“N+H+R”) setting. Zoom-in for best view.

deraining tasks, it does not perform as well as the best task-specific methods (*i.e.*, HI-Diff [72] and Retinexformer [15]) and the best general methods (*i.e.*, FSNet [21] and MIRNet [76]) on deblurring and low-light enhancement tasks. This

may be due to the fact that our method does not explicitly explore frequency domain information and illumination models, making it less effective in capturing critical degradation features, as well as handling a wide range of light intensities

TABLE III

PERFORMANCE COMPARISON IN ALL-IN-ONE (“N+H+R+B+L”) SETTING WITH STATE-OF-THE-ARTS TASK-SPECIFIC, GENERAL, AND ALL-IN-ONE IMAGE RESTORATION METHODS. FOLLOW [34], DENOISING RESULTS ARE REPORTED FOR THE NOISE LEVEL $\sigma = 25$. THE REPORTED RESULTS ARE PARTIALLY BASED ON IDR [34]. * DENOTES A MODEL THAT HAS BEEN RETRAINED.

Type	Method	Denoising	Dehazing	Deraining	Deblurring	Low-light	Average	Params (M)
		CBSD68 [61]	SOTS [64]	Rain100L [65]	GoPro [11]	LOL [13]		
Specific	(AAAI'23) ADFNet* [70]	31.15/0.882	24.18/0.928	32.97/0.943	25.79/0.781	21.15/0.823	27.05/0.871	7.65
	(TIP'23) DehazeFormer* [6]	30.89/0.880	25.31/0.937	33.68/0.954	25.93/0.785	21.31/0.819	27.42/0.875	25.44
	(CVPR'23) DRSformer* [9]	30.97/0.881	24.66/0.931	33.45/0.953	25.56/0.780	21.77/0.821	27.28/0.873	33.72
	(NeurIPS'23) HI-Diff* [72]	30.61/0.878	25.09/0.935	33.26/0.951	26.48/0.800	22.01/0.822	27.49/0.877	23.99
	(ICCV'23) Retinexformer* [15]	30.84/0.880	24.81/0.933	32.68/0.940	25.09/0.779	22.76/0.834	27.24/0.873	1.61
General	(ICCVW'21) SwinIR [17]	30.59/0.868	21.50/0.891	30.78/0.923	24.52/0.773	17.81/0.723	25.04/0.835	0.91
	(TPAMI'22) MIRNet-v2 [18]	30.97/0.881	24.03/0.927	33.89/0.954	26.30/0.799	21.52/0.815	27.34/0.875	5.86
	(CVPR'22) DGUNet [38]	31.10/0.883	24.78/0.940	36.62/0.971	27.25/0.837	21.87/0.823	28.32/0.891	17.33
	(CVPR'22) Restormer [20]	31.49/0.884	24.09/0.927	34.81/0.962	27.22/0.829	20.41/0.806	27.60/0.881	26.13
	(ECCV'22) NAFNet [19]	31.02/0.883	25.23/0.939	35.56/0.967	26.53/0.808	20.49/0.809	27.76/0.881	17.11
	(TPAMI'23) FSNet* [21]	31.33/0.883	25.53/0.943	36.07/0.968	28.32/0.869	22.29/0.829	28.71/0.898	13.28
	(ECCV'24) MambaIR* [40]	31.41/0.884	25.81/0.944	36.55/0.971	28.61/0.875	22.49/0.832	28.97/0.901	26.78
All-in-One	(TPAMI'19) DL [71]	23.09/0.745	20.54/0.826	21.96/0.762	19.86/0.672	19.83/0.712	21.05/0.743	2.09
	(ECCV'22) TAPE [33]	30.18/0.855	22.16/0.861	29.67/0.904	24.47/0.763	18.97/0.621	25.09/0.801	1.07
	(CVPR'22) Transweather [73]	29.00/0.841	21.32/0.885	29.43/0.905	25.12/0.757	21.21/0.792	25.22/0.836	37.93
	(CVPR'22) AirNet [23]	30.91/0.882	21.04/0.884	32.98/0.951	24.35/0.781	18.18/0.735	25.49/0.846	8.93
	(CVPR'23) IDR [34]	31.60/0.887	25.24/0.943	35.63/0.965	27.87/0.846	21.34/0.826	28.34/0.893	15.34
	(NeurIPS'23) PromptIR* [26]	31.47/0.886	26.54/0.949	36.37/0.970	28.71/0.881	22.68/0.832	29.15/0.904	32.96
	(IJCV'24) Gridformer* [37]	31.45/0.885	26.79/0.951	36.61/0.971	29.22/0.884	22.59/0.831	29.33/0.904	34.07
	(ECCV'24) InstructIR [28]	31.40/0.887	27.10/0.956	36.84/0.973	29.40/0.886	23.00/0.836	29.55/0.907	15.80
	Perceive-IR (Ours)	31.44/0.887	28.19/0.964	37.25/0.977	29.46/0.886	22.88/0.833	29.84/0.909	42.02

TABLE IV

DENOISING PERFORMANCE COMPARISON IN THE ONE-BY-ONE SETTING ON DENOISING TASK. \diamond , \diamond , AND \diamond DENOTE TASK-SPECIFIC, GENERAL, AND ALL-IN-ONE IMAGE RESTORATION METHODS, RESPECTIVELY. THE RESULTS IN THE TABLE ARE MAINLY BASED ON IDR [34].

Method	CBSD68 [61]			Urban100 [62]			Kodak24 [63]		
	15	25	50	15	25	50	15	25	50
\diamond DnCNN [1]	33.90	31.24	27.95	32.98	30.81	27.59	34.60	32.14	28.95
\diamond FFDNet [2]	33.87	31.21	27.96	33.83	31.40	28.05	34.63	32.13	28.98
\diamond BRDNet [3]	34.10	31.43	28.16	34.42	31.99	28.56	34.70	32.17	28.99
\diamond ADFNet* [70]	34.21	31.60	28.19	34.50	32.13	28.71	34.77	32.22	29.06
\diamond SwinIR [17]	33.31	30.59	27.13	32.79	30.18	26.52	33.89	31.32	27.93
\diamond MIRNet-v2 [18]	33.66	30.97	27.66	33.30	30.75	27.22	34.29	31.81	28.55
\diamond DGUNet [38]	33.85	31.10	27.92	33.67	31.27	27.94	34.56	32.10	28.91
\diamond Restormer [20]	34.03	31.49	28.11	33.72	31.26	28.03	34.78	32.37	29.08
\diamond NAFNet [19]	33.67	31.02	27.73	33.14	30.64	27.20	34.27	31.80	28.62
\diamond FSNet* [21]	34.09	31.55	28.12	33.88	31.31	28.07	34.75	32.38	29.10
\diamond TAPE [33]	32.86	30.18	26.63	32.19	29.65	25.87	33.24	30.70	27.19
\diamond AirNet [23]	34.14	31.48	28.23	34.40	32.10	28.88	34.81	32.44	29.10
\diamond IDR [34]	34.11	31.60	28.14	33.82	31.29	28.07	34.78	32.42	29.13
\diamond PromptIR [26]	34.34	31.71	28.49	34.77	32.49	29.39	-	-	-
\diamond Perceive-IR	34.38	31.74	28.53	34.86	32.55	29.42	34.84	32.50	29.16

and illumination conditions. Additionally, the use of Restormer as a generator of “medium” quality images during the prompt learning stage might interfere with the learning process on the deblurring and low-light enhancement tasks. Despite producing images of decent quality, they do not match the mediocre quality expected, which affects the restoration performance in these tasks. Despite these limitations, our Perceive-IR consistently outperforms SOTA all-in-one methods across five tasks under One-by-One setting.

D. Visual Results

Figs. 5-6 present the restoration results obtained by state-of-the-art all-in-one methods for both All-in-One (“N+H+R”) and One-by-One setting. In noisy scenarios, Perceive-IR produces clear and sharp denoised outputs, preserving fine textures compared to AirNet [23], PromptIR [26], and InstructIR [28] (e.g., the head and stomach texture parts in rows 1 and 2 of

TABLE V

PERFORMANCE COMPARISON IN THE ONE-BY-ONE SETTING ON DEHAZING, DERAINING, DEBLURRING, AND LOW-LIGHT ENHANCEMENT TASKS. \diamond , \diamond , AND \diamond DENOTE TASK-SPECIFIC, GENERAL, AND ALL-IN-ONE IMAGE RESTORATION METHODS, RESPECTIVELY. THE BEST OVERALL RESULTS ARE MARKED WITH BOLD AND THE BEST RESULTS FROM EACH METHOD CATEGORY ARE IN BOLD.

Method	Dehazing SOTS [64]	Method	Deraining Rain100L [65]
\diamond DehazeNet [4]	22.46/0.851	\diamond UMR [7]	32.39/0.921
\diamond AODNet [74]	20.29/0.877	\diamond MSPFN [8]	33.50/0.948
\diamond FDGAN [5]	23.15/0.921	\diamond LPNet [69]	33.61/0.958
\diamond DehazeFormer* [6]	31.78/0.977	\diamond DRSformer* [9]	38.14/0.983
\diamond Restormer [20]	30.87/0.969	\diamond Restormer [20]	36.74/0.978
\diamond NAFNet* [19]	30.98/0.970	\diamond NAFNet* [19]	36.63/0.977
\diamond FSNet* [21]	31.11/0.971	\diamond FSNet* [21]	37.27/0.980
\diamond AirNet [23]	23.18/0.900	\diamond AirNet [23]	34.90/0.977
\diamond PromptIR [26]	31.31/0.973	\diamond PromptIR [26]	37.04/0.979
\diamond Perceive-IR	31.65/0.977	\diamond Perceive-IR	38.41/0.984
Method	Deblurring GoPro [11]	Method	Low-light LOL [13]
\diamond Nah <i>et al.</i> [11]	29.08/0.914	\diamond Retinex-Net [13]	16.77/0.560
\diamond DeblurGAN [10]	28.70/0.858	\diamond URetinex [14]	21.33/0.835
\diamond Stripformer [12]	33.08/0.962	\diamond SMG [75]	23.81/0.809
\diamond HI-Diff [72]	33.33/0.964	\diamond Retinexformer [15]	25.16/0.845
\diamond MPRNet [16]	32.66/0.959	\diamond MIRNet [76]	24.14/0.835
\diamond Restormer [20]	32.92/0.961	\diamond Restormer [20]	22.43/0.823
\diamond FSNet [21]	33.29/0.963	\diamond DiffIR [22]	23.15/0.828
\diamond AirNet* [23]	31.64/0.945	\diamond AirNet* [23]	21.07/0.811
\diamond PromptIR* [26]	32.41/0.956	\diamond PromptIR* [26]	22.55/0.826
\diamond Perceive-IR	32.83/0.960	\diamond Perceive-IR	23.24/0.838

Fig. 5). In challenging hazy scenes, as seen in row 3, AirNet and PromptIR generate results with low color fidelity, while InstructIR produces blurrier results. In row 4, these comparison methods generate results with additional offsets. Conversely,

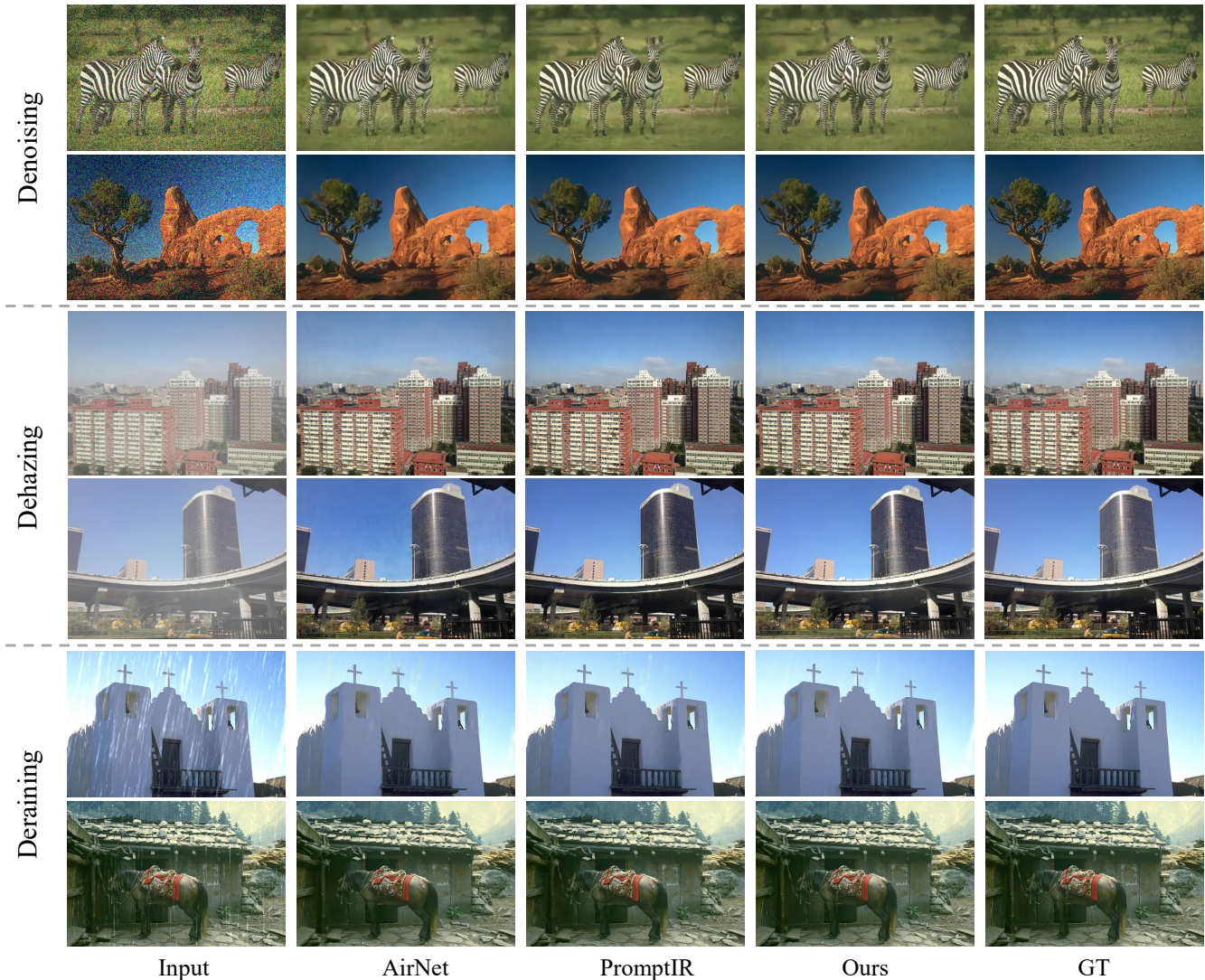


Fig. 6. Visual comparisons of Perceive-IR with state-of-the-art all-in-one methods for One-by-One setting. Zoom-in for best view.

TABLE VI

EFFECTIVENESS OF DIFFERENT COMPONENTS ON THE RAIN100L [65] DATASET.

Index	Prompt	DINO-v2	PGM	CFE	PSNR \uparrow	SSIM \uparrow
(a)	\times	\times	\times	\times	37.15	0.975
(b)	\checkmark	\times	\times	\times	37.37	0.979
(c)	\times	\checkmark	\times	\times	37.32	0.979
(d)	\times	\times	\checkmark	\times	37.28	0.978
(e)	\times	\times	\times	\checkmark	37.23	0.977
(f)	\checkmark	\checkmark	\times	\times	37.52	0.981
(g)	\times	\times	\checkmark	\checkmark	37.38	0.979
(h)	\times	\checkmark	\checkmark	\checkmark	37.45	0.979
(i)	\checkmark	\times	\checkmark	\checkmark	37.50	0.980
(j)	\checkmark	\checkmark	\checkmark	\checkmark	37.76	0.982

the results generated by our method maintain good color and structural integrity. In deraining task, as shown in the iron-frame region in row 6, both AirNet, PromptIR, and InstructIR introduced additional artifacts. In contrast, our approach produced more realistic result. The same trend is illustrated in Fig. 6. These findings demonstrate the effectiveness of our method.

E. Ablation Study

We conduct several ablation experiments to demonstrate the effectiveness of each component in the proposed Perceive-IR.

TABLE VII

EFFECTIVENESS OF THE DIFFERENT LOSS FUNCTIONS ON THE RAIN100L [65] DATASET.

Index	\mathcal{L}_{clip}	\mathcal{L}_{dpl}	\mathcal{L}_{cl}	PSNR \uparrow	SSIM \uparrow
(a)	\times	\times	\times	37.30	0.978
(b)	\checkmark	\times	\times	37.51	0.980
(c)	\times	\checkmark	\times	37.42	0.979
(d)	\times	\times	\checkmark	37.37	0.979
(e)	\times	\checkmark	\checkmark	37.46	0.979
(f)	\checkmark	\checkmark	\times	37.61	0.981
(g)	\checkmark	\times	\checkmark	37.55	0.981
(h)	\checkmark	\checkmark	\checkmark	37.76	0.982

All ablation experiments are performed on the image deraining task (Rain100L [65]) by training models for 100K iterations except for special instructions.

Effects of Different Components. As shown in Tab. VI, we evaluate the effectiveness of various components through a comparison with baseline method (index a) that excludes our modules. The baseline adopts Restormer [20] as its backbone. ‘‘Prompt’’ denotes the prompt learning stage. Specifically, without prompt learning and DINO-v2 (index g), the average PSNR performance is reduced by 0.38 dB. Similarly, without PGM and CFE (index f), the performance is reduced by 0.24 dB. When compared to other modules, the improvement

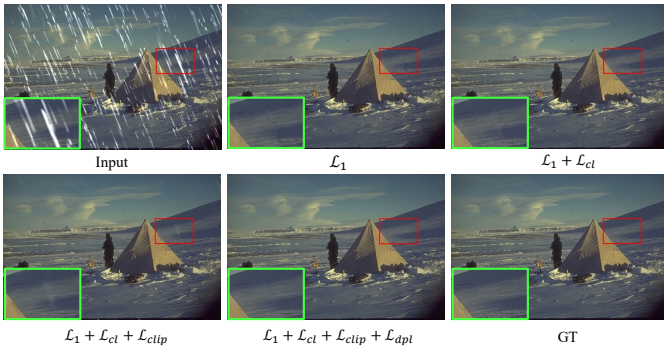


Fig. 7. Visual comparison of the restored images obtained using the individual loss schemes and the proposed scheme.

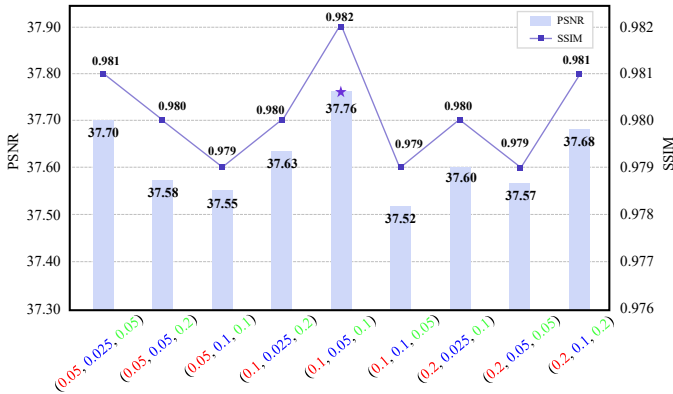


Fig. 8. Comparison of PSNR and SSIM with different weight between different loss function on the Rain100L [65] dataset. red, blue, and green are the weights λ_1 , λ_2 , and λ_3 in Eq. 13, respectively.

brought by prompt learning is more significant, as shown in (index b-e). This suggests that the proposed CLIP-based prompt learning strategy is crucial to the performance. Overall, our model (index j) achieves a significant average PSNR improvement of 0.61 dB than baseline, which is attributed to the effectiveness of each proposed component.

Effects of Different Loss Functions. As shown in Tab. VII, we determine the effectiveness of Perceive-IR under different loss functions. The baseline (index a) use only pixel-level reconstruction loss \mathcal{L}_{rec} . Specifically, compared to the baseline, the approach incorporating \mathcal{L}_{clip} , \mathcal{L}_{dpl} , and \mathcal{L}_{cl} simultaneously achieves a PSNR improvement of 0.46 dB. Furthermore, by integrating the perceptual capabilities of CLIP, the utilization of \mathcal{L}_{clip} (index b) results in PSNR improvement of 0.09 dB and 0.14 dB, respectively, over the use of \mathcal{L}_{dpl} (index c) and \mathcal{L}_{cl} (index d) alone. These findings demonstrate that combining multiple loss functions and leveraging CLIP’s perceptual properties can significantly elevate the quality of image restoration. Fig. 7 illustrates the visual results of various schemes using individual loss modules and our proposed scheme. As the proposed loss modules are successively added, the restored image more closely resembles the ground truth.

In addition, we further explored the effect of weights between different loss functions. As shown in Fig. 8, peak performance is observed around $(\lambda_1, \lambda_2, \lambda_3) = (0.1, 0.05, 0.1)$. Similarly, sub-optimal performance is obtained when λ_1 and λ_3 are larger than λ_2 , e.g., $(0.05, 0.025, 0.05)$ and $(0.2, 0.1, 0.2)$. In other cases, the performance degradation is more significant. Thus, in our method, λ_1 , λ_2 , and λ_3 are set as 0.1,

0.05, and 0.1, respectively.

Effects of Prompt Number and Initialization Schemes In this study, we examine the impacts of different prompt number and prompt initialization settings. We consider three scenarios: two, three, and four pairs of prompt-image. Specifically, we explore three configurations for prompt initialization, **i)** Fixed: The prompts are fixed throughout the entire training process. **ii)** Random initialization: The prompts are initially randomized and then learned from there. **iii)** Partial random initialization: Part of the token is initialized randomly while one token is fixed as a specific word. For example, a five-token prompt is initialized as “ \times , \times , \times , \times , excellent”, where “ \times ” denotes random initialization. And the entire prompt is updated during prompt learning.

As shown in Table VIII, using three prompts in the CLIP model, with the same initialization strategy, outperforms using two or four prompts. The use of two prompt-image pairs may result in inadequate model discrimination, while four pairs could offer too much detail, negatively affecting the portrayal of image quality. This suggests that an appropriate number of prompts is beneficial in providing a more precise guide for the restoration process. In all prompt configurations, “Partial random initialization” consistently outperforms both “Fixed” and “Random initialization”. The use of fixed or random prompts can lead to performance degradation due to the domain gap between the pre-training data of the CLIP model and the specifics of our task. Random prompts slightly enhance performance by easing learning constraints compared with fixed prompts. Therefore, the partial random initialization strategy achieves optimal results, likely because it provides more effective guidance and ensuring ample learning space across various prompt scenarios. We additionally consider the formulation of the specified words. As seen in (index g, i) and (index l, m), such vague definitions are prone to appear in the data of the pre-trained model, which reduces the performance. When the prompt and image quality do not align, as in (index h, i), it disrupts the prompt learning stage, leading to a significant drop in performance. In all, our scheme (index i) achieves the best results and proves its superiority.

Effects of Different Combinations of Degradation. In this study, we assess the performance of Perceive-IR under various combinations of degradation types. As demonstrated in Tab. IX, the performance of the model is optimal on a single task. With the number of tasks incremented, the performance of each task oscillates below the optimal value. In addition, there may be some interesting phenomena under different combinations of degradation. For example, models trained in the “N+H+L” setting show superior performance in denoising and dehazing compared to those trained in the “N+H+B” setting. Similarly, models trained in the “N+H+R+L” setting has better performance on denoising and dehazing than models trained in the “N+H+R+B” setting, but worse performance on the deraining task. This may be due to the distribution of low-light images may contain more noise and haze-like artifacts, which can enhance the model’s ability to handle these types of degradation. On the other hand, deraining requires specific features related to rain streaks, which might not be as prevalent in low-light conditions.

TABLE VIII
PERFORMANCE COMPARISONS ON THE RAIN100L [65] DATASET AMONG DIFFERENT PROMPT INITIALIZATION SETTINGS FOR THE CLIP MODEL.

Type	Index	Prompt Setting	PSNR↑	SSIM↑
Two pairs of prompt-image	(a)	Fixed (“excellent”/“terrible”)	37.36	0.979
	(b)	Random initialization	37.49	0.980
	(c)	Partial random initialization (“excellent”/“terrible”)	37.56	0.981
Three pairs of prompt-image	(d)	Fixed (“excellent”/“mediocre”/“terrible”)	37.45	0.979
	(e)	Fixed (“good”/“moderate”/“bad”)	37.50	0.980
	(f)	Random initialization	37.52	0.981
	(g)	Partial random initialization (“good”/“moderate”/“bad”)	37.68	0.982
	(h)	Partial random initialization (“terrible”/“moderate”/“excellent”)	37.43	0.979
	(i)	Partial random initialization (“excellent”/“mediocre”/“terrible”) (Ours)	37.76	0.982
Four pairs of prompt-image	(j)	Fixed (“excellent”/“slightly better”/“slightly worse”/“terrible”)	37.44	0.979
	(k)	Random initialization	37.56	0.981
	(l)	Partial random initialization (“excellent”/“good”/“bad”/“terrible”)	37.63	0.982
	(m)	Partial random initialization (“excellent”/“slightly better”/“slightly worse”/“terrible”)	37.67	0.982

TABLE IX
PERFORMANCE OF THE PROPOSED PERCEIVE-IR, WHEN CONDUCTED ON VARIOUS COMBINATIONS OF DEGRADATION TYPES. NUMBER OF COMBINATIONS OF TASKS FROM 1 TO 5.

Degradation					Denoising (CBSD68 [61])			Dehazing	Deraining	Deblurring	Low-light
N	H	R	B	L	$\sigma = 15$	$\sigma = 25$	$\sigma = 50$	SOTS [64]	Rain100L [65]	GoPro [11]	LOL [13]
✓	✗	✗	✗	✗	34.38/0.939	31.74/0.898	28.53/0.813	-	-	-	-
✗	✓	✗	✗	✗	-	-	-	31.65/0.977	-	-	-
✗	✗	✓	✗	✗	-	-	-	-	38.41/0.984	-	-
✗	✗	✗	✓	✗	-	-	-	-	-	32.83/0.960	-
✗	✗	✗	✗	✓	-	-	-	-	-	-	23.24/0.838
✓	✓	✗	✗	✗	34.35/0.939	31.70/0.897	28.46/0.812	30.79/0.975	-	-	-
✓	✗	✓	✗	✗	34.31/0.937	31.66/0.895	28.41/0.810	-	38.11/0.980	-	-
✗	✓	✓	✗	✗	-	-	-	30.92/0.976	38.23/0.981	-	-
✗	✗	✗	✓	✓	-	-	-	-	-	32.33/0.953	22.97/0.835
✓	✓	✓	✗	✗	34.13/0.934	31.53/0.890	28.31/0.804	30.87/0.975	38.29/0.980	-	-
✓	✓	✗	✓	✗	34.16/0.934	31.55/0.890	28.32/0.803	30.11/0.972	-	31.29/0.934	-
✓	✓	✗	✗	✓	34.20/0.935	31.57/0.891	28.33/0.804	30.36/0.973	-	-	22.90/0.834
✓	✓	✓	✓	✗	34.11/0.932	31.50/0.888	28.26/0.802	28.87/0.967	37.83/0.979	30.31/0.911	-
✓	✓	✓	✗	✓	34.13/0.933	31.52/0.889	28.27/0.802	29.62/0.970	37.49/0.978	-	22.76/0.831
✓	✓	✗	✓	✓	34.10/0.932	31.48/0.888	28.25/0.801	29.23/0.968	-	29.89/0.897	22.81/0.834
✓	✓	✓	✓	✓	34.04/0.931	31.44/0.887	28.19/0.801	28.19/0.964	37.25/0.977	29.46/0.886	22.88/0.833

Effects of Restoration Models for Prompt Learning. In this part, we explore the effects of different restoration methods during the prompt learning stage. As shown in Tab. X, the better all-in-one restoration model like PromptIR [26] yields poorer results than AirNet [23], and superior general restoration model like Restormer [20] perform better than MPRNet [16]. These observations may be attributed to two factors. Firstly, the quality of images restored by PromptIR surpasses the “mediocre” standard, which lead to confusion during prompt learning and potentially undermine performance. Secondly, as these restoration methods generate images of notably high quality, the prompt “mediocre” may converge towards the prompt “excellent”. This convergence could diminish the effectiveness of the “mediocre” prompt, reducing the distinctiveness of the three prompts to essentially two. When comparing Restormer and MPRNet, the opposite effect is observed on the relatively poorer MPRNet. In summary, the “medium” quality image restored by appropriate restoration method are more beneficial for the prompt learning stage.

TABLE X
PERFORMANCE COMPARISONS ON THE RAIN100L [65] DATASET AMONG DIFFERENT RESTORATION MODELS FOR THE PROMPT LEARNING STAGE.

Method	PSNR↑	SSIM↑
Perceive-IR (MPRNet [16])	37.68	0.982
Perceive-IR (AirNet [23])	37.64	0.981
Perceive-IR (PromptIR [26])	37.57	0.981
Perceive-IR (Restormer [20]) (Ours)	37.76	0.982

TABLE XI
PERFORMANCE COMPARISONS ON UNSEEN NOISE LEVEL OF $\sigma = 60, 100$.

Method	CBSD68 [61]		Urban100 [62]	
	$\sigma = 60$	$\sigma = 100$	$\sigma = 60$	$\sigma = 100$
AirNet [23]	26.01	14.29	25.11	14.23
PromptIR [26]	26.71	20.23	27.24	20.94
Perceive-IR	27.11	20.67	27.59	21.52

F. Generalization

Follow [26], we utilize the all-in-one methods trained under the noise levels of $\sigma \in \{15, 25, 50\}$ to test on the unseen noise levels of $\sigma \in \{60, 100\}$. In addition, we evaluate the performance of these methods under “N+H+R+B+L” setting, specifically focusing on the training-unseen underwater enhancement

TABLE XII

PERFORMANCE COMPARISONS ON TRAINING-UNSEEN UNDERWATER IMAGE ENHANCEMENT TASK. WE USE THE ALL-IN-ONE METHODS (PRE-TRAINED UNDER “N+H+R+B+L” TRAINING SETTING) TO DIRECTLY TEST ON THE UIEB [77] DATASET. THE PROMPT USED IN INSTRUCTIR [28] IS “This underwater image is poor, please enhance it.”.

Method	UIEB [77]			C60 [77]	
	PSNR \uparrow	SSIM \uparrow	LPIPS \downarrow	UCIQE \uparrow	UIQM \uparrow
PromptIR [26]	20.19	0.827	0.256	0.527	2.305
Gridformer [37]	20.48	0.846	0.243	0.540	2.517
InstructIR [28]	21.07	0.872	0.189	0.552	2.489
Perceive-IR	21.75	0.891	0.168	0.561	2.558

TABLE XIII

PERFORMANCE COMPARISONS OF PERCEIVE-IR WITH DIFFERENT RESTORATION BACKBONES UNDER THE “N+H+R” AND “N+H+R+B+L” TRAINING SETTINGS VERSUS STATE-OF-THE-ART ALL-IN-ONE IMAGE RESTORATION METHODS.

Method	N+H+R		N+H+R+B+L		Params (M)
	PSNR \uparrow	SSIM \uparrow	PSNR \uparrow	SSIM \uparrow	
AirNet [23]	31.20	0.910	25.49	0.846	8.93
PromptIR [26]	32.06	0.913	29.15	0.904	32.96
InstructIR [28]	32.43	0.913	29.55	0.907	15.80
Perceive-IR_{NAFNet}	32.52	0.915	29.71	0.908	21.73
Perceive-IR_{Restormer}	32.63	0.917	29.84	0.909	42.02

task. Tabs. XI and XII show that our Perceive-IR outperforms other all-in-one methods on both unseen noise levels and the unseen task, demonstrates superior generalization capability.

G. Discussion and Limitation

To validate the adaptation of our method with different restoration backbone, we using NAFNet as the backbone in the restoration stage. As demonstrated in the Tab. XIII, Perceive-IR_{NAFNet} outperforms the state-of-the-art all-in-one methods such as PromptIR [26] and InstructIR [28], by achieving an average PSNR that is 0.46/0.56 dB and 0.09/0.16 dB higher under “N+H+R” and “N+H+R+B+L” settings, respectively. Note that the number of parameters in Perceive-IR depends heavily on the chosen backbone model, as shown in Perceive-IR_{NAFNet} and Perceive-IR_{Restormer}. This suggests that our approach has the potential to serve as a more lightweight solution and could be integrated as a plug-and-play module into more advanced restoration models in the future.

Although our Perceive-IR has achieved superior generalization ability and scalability in addressing multiple degradation, its flexibility in blind real-world conditions may be limited. Moreover, while Perceive-IR demonstrates superiority over the state-of-the-art all-in-one and general image restoration methods, it still falls short when compared to the most advanced state-of-the-art task-specific methods, particularly in tasks such as deblurring, and low-light enhancement. Lastly, the interrelationships among the various degradation are not sufficiently clear, for example, as shown in Tab. IX, the model performs better on the dehazing task in the “N+H+R+B” setting compared to the “N+H+R+L” setting, yet the deraining performance is degraded.

V. CONCLUSION

This paper proposes Perceive-IR, an approach for learning to perceive degradation better for all-in-one image restoration. Specifically, we leverage prompt learning technique to acquire a fine-grained quality perceiver capable of distinguishing three-tier quality levels by constraining the prompt-image similarity in the CLIP perception space. In addition, we fully

leverage pre-trained large vision models (e.g., DINO-v2) to construct semantic guidance module to perceive the reliable content to promote the restoration process. Finally, we introduce a quality-aware learning strategy along with difficulty-adaptive perceptual loss to realize fine-grained quality control. Extensive experiments have demonstrated that our Perceive-IR achieves state-of-the-art results on all-in-one image restoration tasks and demonstrates its superior generalisation ability when dealing with unseen tasks.

REFERENCES

- [1] K. Zhang, W. Zuo, Y. Chen, D. Meng, and L. Zhang, “Beyond a gaussian denoiser: Residual learning of deep cnn for image denoising,” *TIP*, vol. 26, no. 7, pp. 3142–3155, 2017.
- [2] K. Zhang, W. Zuo, and L. Zhang, “Ffdnet: Toward a fast and flexible solution for cnn-based image denoising,” *TIP*, vol. 27, no. 9, pp. 4608–4622, 2018.
- [3] C. Tian, Y. Xu, and W. Zuo, “Image denoising using deep cnn with batch renormalization,” *MN*, vol. 121, pp. 461–473, 2020.
- [4] B. Cai, X. Xu, K. Jia, C. Qing, and D. Tao, “Dehazenet: An end-to-end system for single image haze removal,” *TIP*, vol. 25, no. 11, pp. 5187–5198, 2016.
- [5] Y. Dong, Y. Liu, H. Zhang, S. Chen, and Y. Qiao, “Fd-gan: Generative adversarial networks with fusion-discriminator for single image dehazing,” in *AAAI*, vol. 34, no. 07, 2020, pp. 10729–10736.
- [6] Y. Song, Z. He, H. Qian, and X. Du, “Vision transformers for single image dehazing,” *TIP*, vol. 32, pp. 1927–1941, 2023.
- [7] R. Yasarla and V. M. Patel, “Uncertainty guided multi-scale residual learning-using a cycle spinning cnn for single image de-raining,” in *CVPR*, 2019, pp. 8405–8414.
- [8] K. Jiang, Z. Wang, P. Yi, C. Chen, B. Huang, Y. Luo, J. Ma, and J. Jiang, “Multi-scale progressive fusion network for single image deraining,” in *CVPR*, 2020, pp. 8346–8355.
- [9] X. Chen, H. Li, M. Li, and J. Pan, “Learning a sparse transformer network for effective image deraining,” in *CVPR*, June 2023, pp. 5896–5905.
- [10] O. Kupyn, V. Budzan, M. Mykhailych, D. Mishkin, and J. Matas, “Deblurgan: Blind motion deblurring using conditional adversarial networks,” in *CVPR*, 2018, pp. 8183–8192.
- [11] S. Nah, T. Hyun Kim, and K. Mu Lee, “Deep multi-scale convolutional neural network for dynamic scene deblurring,” in *CVPR*, 2017, pp. 3883–3891.
- [12] F.-J. Tsai, Y.-T. Peng, Y.-Y. Lin, C.-C. Tsai, and C.-W. Lin, “Stripformer: Strip transformer for fast image deblurring,” in *ECCV*, 2022, pp. 146–162.
- [13] C. Wei, W. Wang, W. Yang, and J. Liu, “Deep retinex decomposition for low-light enhancement,” in *BMVC*, 2018.
- [14] W. Wu, J. Weng, P. Zhang, X. Wang, W. Yang, and J. Jiang, “Uretinex-net: Retinex-based deep unfolding network for low-light image enhancement,” in *CVPR*, 2022, pp. 5901–5910.
- [15] Y. Cai, H. Bian, J. Lin, H. Wang, R. Timofte, and Y. Zhang, “Retinex-former: One-stage retinex-based transformer for low-light image enhancement,” in *ICCV*, 2023.
- [16] S. W. Zamir, A. Arora, S. Khan, M. Hayat, F. S. Khan, M.-H. Yang, and L. Shao, “Multi-stage progressive image restoration,” in *CVPR*, 2021, pp. 14816–14826.
- [17] J. Liang, J. Cao, G. Sun, K. Zhang, L. Van Gool, and R. Timofte, “Swinir: Image restoration using swin transformer,” in *ICCV*, 2021, pp. 1833–1844.
- [18] S. W. Zamir, A. Arora, S. Khan, M. Hayat, F. S. Khan, M.-H. Yang, and L. Shao, “Learning enriched features for fast image restoration and enhancement,” *TPAMI*, vol. 45, no. 2, pp. 1934–1948, 2022.
- [19] L. Chen, X. Chu, X. Zhang, and J. Sun, “Simple baselines for image restoration,” in *ECCV*, 2022, pp. 17–33.
- [20] S. W. Zamir, A. Arora, S. Khan, M. Hayat, F. S. Khan, and M.-H. Yang, “Restormer: Efficient transformer for high-resolution image restoration,” in *CVPR*, 2022, pp. 5728–5739.
- [21] Y. Cui, W. Ren, X. Cao, and A. Knoll, “Image restoration via frequency selection,” *TPAMI*, 2023.
- [22] B. Xia, Y. Zhang, S. Wang, Y. Wang, X. Wu, Y. Tian, W. Yang, and L. Van Gool, “Diffir: Efficient diffusion model for image restoration,” in *ICCV*, 2023, pp. 13095–13105.
- [23] B. Li, X. Liu, P. Hu, Z. Wu, J. Lv, and X. Peng, “All-in-one image restoration for unknown corruption,” in *CVPR*, 2022, pp. 17452–17462.

- [24] D. Park, B. H. Lee, and S. Y. Chun, "All-in-one image restoration for unknown degradations using adaptive discriminative filters for specific degradations," in *CVPR*, 2023, pp. 5815–5824.
- [25] J. Ma, T. Cheng, G. Wang, Q. Zhang, X. Wang, and L. Zhang, "Prores: Exploring degradation-aware visual prompt for universal image restoration," *arXiv preprint arXiv:2306.13653*, 2023.
- [26] V. Potlapalli, S. W. Zamir, S. Khan, and F. S. Khan, "Promptir: Prompting for all-in-one blind image restoration," in *NeurIPS*, 2023, pp. 71 275–71 293.
- [27] X. Lin, C. Ren, K. C. Chan, L. Qi, J. Pan, and M.-H. Yang, "Multi-task image restoration guided by robust dino features," *arXiv preprint arXiv:2312.01677*, 2023.
- [28] M. V. Conde, G. Geigle, and R. Timofte, "High-quality image restoration following human instructions," in *ECCV*, 2024.
- [29] Z. Luo, F. K. Gustafsson, Z. Zhao, J. Sjölund, and T. B. Schön, "Controlling vision-language models for universal image restoration," *arXiv preprint arXiv:2310.01018*, 2023.
- [30] A. Radford, J. W. Kim, C. Hallacy, A. Ramesh, G. Goh, S. Agarwal, G. Sastry, A. Askell, P. Mishkin, J. Clark *et al.*, "Learning transferable visual models from natural language supervision," in *ICLR*, 2021, pp. 8748–8763.
- [31] M. Caron, H. Touvron, I. Misra, H. Jégou, J. Mairal, P. Bojanowski, and A. Joulin, "Emerging properties in self-supervised vision transformers," in *ICCV*, 2021, pp. 9650–9660.
- [32] Z. Tan, Y. Wu, Q. Liu, Q. Chu, L. Lu, J. Ye, and N. Yu, "Exploring the application of large-scale pre-trained models on adverse weather removal," *TIP*, vol. 33, pp. 1683–1698, 2024.
- [33] L. Liu, L. Xie, X. Zhang, S. Yuan, X. Chen, W. Zhou, H. Li, and Q. Tian, "Tape: Task-agnostic prior embedding for image restoration," in *ECCV*, 2022, pp. 447–464.
- [34] J. Zhang, J. Huang, M. Yao, Z. Yang, H. Yu, M. Zhou, and F. Zhao, "Ingredient-oriented multi-degradation learning for image restoration," in *CVPR*, 2023, pp. 5825–5835.
- [35] M. Yao, R. Xu, Y. Guan, J. Huang, and Z. Xiong, "Neural degradation representation learning for all-in-one image restoration," *arXiv preprint arXiv:2310.12848*, 2023.
- [36] Y.-W. Chen and S.-C. Pei, "Always clear days: Degradation type and severity aware all-in-one adverse weather removal," *arXiv preprint arXiv:2310.18293*, 2023.
- [37] G. R. dense transformer with grid structure for image restoration in adverse weather conditions, "Gridformer: Residual dense transformer with grid structure for image restoration in adverse weather conditions," *IJCV*, pp. 1–23, 2024.
- [38] C. Mou, Q. Wang, and J. Zhang, "Deep generalized unfolding networks for image restoration," in *CVPR*, 2022, pp. 17 399–17 410.
- [39] C. Wang, J. Pan, W. Wang, J. Dong, M. Wang, Y. Ju, and J. Chen, "Promptrestorer: A prompting image restoration method with degradation perception," in *NeurIPS*, 2023, pp. 8898–8912.
- [40] H. Guo, J. Li, T. Dai, Z. Ouyang, X. Ren, and S.-T. Xia, "Mambair: A simple baseline for image restoration with state-space model," in *ECCV*, 2024.
- [41] T. Brown, B. Mann, N. Ryder, M. Subbiah, J. D. Kaplan, P. Dhariwal, A. Neelakantan, P. Shyam, G. Sastry, A. Askell *et al.*, "Language models are few-shot learners," in *NeurIPS*, 2020, pp. 1877–1901.
- [42] X. Liu, K. Ji, Y. Fu, W. L. Tam, Z. Du, Z. Yang, and J. Tang, "P-tuning v2: Prompt tuning can be comparable to fine-tuning universally across scales and tasks," *arXiv preprint arXiv:2110.07602*, 2021.
- [43] Y. Lu, J. Liu, Y. Zhang, Y. Liu, and X. Tian, "Prompt distribution learning," in *CVPR*, 2022, pp. 5206–5215.
- [44] M. Jia, L. Tang, B.-C. Chen, C. Cardie, S. Belongie, B. Hariharan, and S.-N. Lim, "Visual prompt tuning," in *ECCV*, 2022, pp. 709–727.
- [45] Q. Huang, X. Dong, D. Chen, W. Zhang, F. Wang, G. Hua, and N. Yu, "Diversity-aware meta visual prompting," in *CVPR*, 2023, pp. 10 878–10 887.
- [46] W. Liu, X. Shen, C.-M. Pun, and X. Cun, "Explicit visual prompting for low-level structure segmentations," in *CVPR*, 2023, pp. 19 434–19 445.
- [47] A. Bar, Y. Gandelsman, T. Darrell, A. Globerson, and A. Efros, "Visual prompting via image inpainting," in *NeurIPS*, vol. 35, 2022, pp. 25 005–25 017.
- [48] A. Hojel, Y. Bai, T. Darrell, A. Globerson, and A. Bar, "Finding visual task vectors," *arXiv preprint arXiv:2404.05729*, 2024.
- [49] Z. Liang, C. Li, S. Zhou, R. Feng, and C. C. Loy, "Iterative prompt learning for unsupervised backlit image enhancement," in *ICCV*, 2023, pp. 8094–8103.
- [50] T. Wei, D. Chen, W. Zhou, J. Liao, Z. Tan, L. Yuan, W. Zhang, and N. Yu, "Hairclip: Design your hair by text and reference image," in *CVPR*, 2022, pp. 18 072–18 081.
- [51] Z. Wang, Y. Lu, Q. Li, X. Tao, Y. Guo, M. Gong, and T. Liu, "Cris: Clip-driven referring image segmentation," in *CVPR*, 2022, pp. 11 686–11 695.
- [52] Y. Rao, W. Zhao, G. Chen, Y. Tang, Z. Zhu, G. Huang, J. Zhou, and J. Lu, "Denseclip: Language-guided dense prediction with context-aware prompting," in *CVPR*, 2022, pp. 18 082–18 091.
- [53] M. Oquab, T. Darcet, T. Moutakanni, H. Vo, M. Szafraniec, V. Khalidov, P. Fernandez, D. Haziza, F. Massa, A. El-Nouby *et al.*, "Dinov2: Learning robust visual features without supervision," *arXiv preprint arXiv:2304.07193*, 2023.
- [54] C. Beilei, I. Mobarakol, B. Long, and R. Hongliang, "Surgical-dino: Adapter learning of foundation model for depth estimation in endoscopic surgery," *arXiv preprint arXiv:2401.06013*, 2024.
- [55] J. Zhang, C. Herrmann, J. Hur, L. Polania Cabrera, V. Jampani, D. Sun, and M.-H. Yang, "A tale of two features: Stable diffusion complements dino for zero-shot semantic correspondence," in *NeurIPS*, vol. 36, 2024.
- [56] H. Wu, Y. Qu, S. Lin, J. Zhou, R. Qiao, Z. Zhang, Y. Xie, and L. Ma, "Contrastive learning for compact single image dehazing," in *CVPR*, 2021, pp. 10 551–10 560.
- [57] Y. Zheng, J. Zhan, S. He, J. Dong, and Y. Du, "Curricular contrastive regularization for physics-aware single image dehazing," in *CVPR*, 2023, pp. 5785–5794.
- [58] K. Simonyan and A. Zisserman, "Very deep convolutional networks for large-scale image recognition," *arXiv preprint arXiv:1409.1556*, 2014.
- [59] P. Arbelaez, M. Maire, C. Fowlkes, and J. Malik, "Contour detection and hierarchical image segmentation," *TPAMI*, vol. 33, no. 5, pp. 898–916, 2010.
- [60] K. Ma, Z. Duanmu, Q. Wu, Z. Wang, H. Yong, H. Li, and L. Zhang, "Waterloo exploration database: New challenges for image quality assessment models," *TIP*, vol. 26, no. 2, pp. 1004–1016, 2016.
- [61] D. Martin, C. Fowlkes, D. Tal, and J. Malik, "A database of human segmented natural images and its application to evaluating segmentation algorithms and measuring ecological statistics," in *ICCV*, vol. 2, 2001, pp. 416–423.
- [62] J.-B. Huang, A. Singh, and N. Ahuja, "Single image super-resolution from transformed self-exemplars," in *CVPR*, 2015, pp. 5197–5206.
- [63] R. Franzen, "Kodak lossless true color image suite," <http://r0k.us/graphics/kodak/>, 1999.
- [64] B. Li, W. Ren, D. Fu, D. Tao, D. Feng, W. Zeng, and Z. Wang, "Benchmarking single-image dehazing and beyond," *TIP*, vol. 28, no. 1, pp. 492–505, 2018.
- [65] W. Yang, R. T. Tan, J. Feng, J. Liu, Z. Guo, and S. Yan, "Deep joint rain detection and removal from a single image," in *CVPR*, 2017, pp. 1357–1366.
- [66] R. Zhang, P. Isola, A. A. Efros, E. Shechtman, and O. Wang, "The unreasonable effectiveness of deep features as a perceptual metric," in *CVPR*, 2018, pp. 586–595.
- [67] M. Yang and A. Sowmya, "An underwater color image quality evaluation metric," *TIP*, vol. 24, no. 12, pp. 6062–6071, 2015.
- [68] K. Panetta, C. Gao, and S. Agaian, "Human-visual-system-inspired underwater image quality measures," *JOE*, vol. 41, no. 3, pp. 541–551, 2015.
- [69] H. Gao, X. Tao, X. Shen, and J. Jia, "Dynamic scene deblurring with parameter selective sharing and nested skip connections," in *CVPR*, 2019, pp. 3848–3856.
- [70] H. Shen, Z.-Q. Zhao, and W. Zhang, "Adaptive dynamic filtering network for image denoising," in *AAAI*, vol. 37, no. 2, 2023, pp. 2227–2235.
- [71] Q. Fan, D. Chen, L. Yuan, G. Hua, N. Yu, and B. Chen, "A general decoupled learning framework for parameterized image operators," *TPAMI*, vol. 43, no. 1, pp. 33–47, 2019.
- [72] Z. Chen, Y. Zhang, L. Ding, X. Bin, J. Gu, L. Kong, and X. Yuan, "Hierarchical integration diffusion model for realistic image deblurring," in *NeurIPS*, 2023.
- [73] J. M. J. Valanarasu, R. Yasarla, and V. M. Patel, "Transweather: Transformer-based restoration of images degraded by adverse weather conditions," in *CVPR*, 2022, pp. 2353–2363.
- [74] B. Li, X. Peng, Z. Wang, J. Xu, and D. Feng, "Aod-net: All-in-one dehazing network," in *ICCV*, 2017, pp. 4770–4778.
- [75] X. Xu, R. Wang, and J. Lu, "Low-light image enhancement via structure modeling and guidance," in *CVPR*, 2023, pp. 9893–9903.
- [76] S. W. Zamir, A. Arora, S. Khan, M. Hayat, F. S. Khan, M.-H. Yang, and L. Shao, "Learning enriched features for real image restoration and enhancement," in *ECCV*, 2020, pp. 492–511.
- [77] C. Li, C. Guo, W. Ren, R. Cong, J. Hou, S. Kwong, and D. Tao, "An underwater image enhancement benchmark dataset and beyond," *TIP*, vol. 29, pp. 4376–4389, 2020.